Ultrasonics 166 (2026) 108106

Contents lists available at ScienceDirect

Ultrasonics

journal homepage: www.elsevier.com/locate/ultras

Numerical modeling of acoustic radiation force on a bubble through layered mediums☆

Xuan Cheng [a], Yuehaiqin Wang [a], Shiyu Li [a], Zhixiong Gong [a,b,*]

[a] State Key Laboratory of Ocean Engineering, School of Ocean and Civil Engineering, Shanghai Jiao Tong University, No. 800 Dongchuan Road, Shanghai, 200240, China

[b] Key Laboratory of Marine Intelligent Equipment and System, Ministry of Education, China

ARTICLE INFO

Keywords:
Single-beam acoustical tweezers
Bubble manipulation
Vortex beam
Acoustic radiation force
Layered mediums

ABSTRACT

Non-contact bubble manipulation with acoustical tweezers has shown significant potential in the field of ultrasound-driven controlled drug delivery and subdiffraction imaging. While these works are implemented recently by experiments, the numerical modeling of the acoustic radiation force (ARF) on a bubble in the real biological environment has not yet been well developed. In this work, we establish the theoretical calculation model for the bubble selective manipulation across the layered mediums of real biological environment and compute it by the derived across-medium ARF calculation method based on the angular spectrum method (ASM). With the consideration of the multiple biological mediums, the value of the axial ARF decreases by two to three times. In this context, this work establishes quantitative models for the ARF acting on a bubble and presents a single-beam three-dimensional (3D) trapping strategy based on focused vortex beams. These results offer practical guidance for designing acoustic fields that enable non-contact bubble manipulation both in vitro and in vivo applications.

1. Introduction

Bubbles, as attractive particles in nature, are widely used in diverse fields such as biomedical science [1–5], ultrasound and subdiffraction imaging [6–10], and materials science [9,11–13]. Given the inherent instability of bubble position and size [14], the non-contact manipulation of bubbles is of great importance.

Based on different physical principles, non-contact manipulation techniques can be categorized into optical tweezers [15,16], magnetic tweezers [17], and acoustic tweezers [18,19], etc. Optical tweezers offer high manipulation precision. However, the use of high intensity lasers can cause thermal damage to particles [20,21], posing bio-safety risks. Magnetic tweezers require target particles to be magnetic; otherwise, magnetic pre-labeling is necessary. These limit their application in biological environments. In contrast, acoustic tweezers exhibit high biocompatibility and have been extensively investigated in the biomedical field for applications such as cell manipulation, sorting, and patterning. Compared to optical tweezers, acoustic tweezers can generate strong forces at lower power levels and are capable of penetrating complex, absorptive mediums like biological tissues. Conventional standing-wave acoustic tweezers lack selective manipulation capability due to the presence of multiple equilibrium positions (i.e., nodes and antinodes). In contrast, single-beam acoustic tweezers, which create a highly localized acoustic field at the focus, are a natural candidate for 3D selective manipulation. Currently, single-beam acoustic tweezers based on focused acoustic vortices have been successfully employed for the selective manipulation of particles such as cells [22,23] and microbubbles [24]. Nevertheless, manipulating the bubble with the acoustic tweezer still presents considerable challenges when across the layered mediums. In the real biological environment, the multilayered mediums including many heterogeneous tissues will weaken and disrupt the acoustic field behind by transmission, refraction and attenuation [25], which may change the trapping ARF characteristics including its amplitude and direction in the acoustic tweezer, and directly impact the control efficiency. Owing to the complexity of the beam propagation across the real multilayered mediums, to date, only some simplified experiment work about the trapping bubble across the real tissue medium

☆ This article is part of a Special issue entitled: 'Ultrasonic-Assisted Microfluidics and Streaming' published in Ultrasonics.

* Corresponding author at: State Key Laboratory of Ocean Engineering, School of Ocean and Civil Engineering, Shanghai Jiao Tong University, No. 800 Dongchuan Road, Shanghai, 200240, China.

E-mail addresses: chengxuan2022@sjtu.edu.cn (X. Cheng), yuehaiqin.wang@sjtu.edu.cn (Y. Wang), shiyu.li@sjtu.edu.cn (S. Li), zhixiong.gong@sjtu.edu.cn (Z. Gong).

URL: https://naoce.sjtu.edu.cn/teachers/12344.html (Z. Gong).

https://doi.org/10.1016/j.ultras.2026.108106
Received 30 November 2025; Received in revised form 22 March 2026; Accepted 17 April 2026
Available online 25 April 2026

has been conducted. For example, based on the experiment method and equipment in the free water, Diego Baresch and Valeria Garbin carried out the trapping bubble experiment across the tissue mimicking material like the tofu, and found a measurable decrease in the trapping force axial ARF consistent with the acoustic properties of the tofu [24]. Moreover, the trapping microbubble experiment within the circulation in vivo was conducted, but only two-dimensional (2D) trap with the lateral ARF was implemented [4]. The numerical modeling of the ARF on a bubble in the real biological environment has not yet been well developed, which is demanded more extensively and efficiently as the reference to the biomedicine experiment and application about non-contact bubble manipulation.

In this paper, we establish the theoretical calculation model for the bubble selective manipulation across the layered mediums of real biological environment which refers to the real multilayered mediums applied to the pancreas treatment simulations by the high focused ultrasound [26] and study the effect of the layered mediums for ARF, especially axial ARF on the bubble when considering the multiple biological mediums like skin, fat and muscle, quantitatively. By means of the trapping calculation for the constructed model using the derived ASM-based ARF calculation method across the layered mediums and comparative analysis with the unified model, we theoretically demonstrate that (i) under the condition of incident focused vortex beam, a similarly single-beam 3D selective acoustic tweezer across the real biological multilayered mediums can be created in the model, which traps the bubble nearly at the axial trap equilibrium position and that (ii) the real biological multilayer mediums can generate great impact on the ARF and the value of the axial trapping ARF on bubble will be attenuated by two to three times under the same incident pressure. This conclusion has importantly referenceable significance for the non-contact bubble manipulation in the real biological environment and guides the design of the acoustic field for this technology's in vitro or in vivo applications.

The paper is organized into four parts. Section 2 briefly describes the acoustic field and ARF calculation formulas based on the ASM and then, derives the ASM-based ARF calculation method across the layered mediums. Sections 3.1 and 3.2 introduce three scenarios about the layered mediums and demonstrate the ASM-based ARF calculation method across the tofu, respectively. The unified numerical model for the trapping calculation on the bubble is established in Section 4.1. Meanwhile, the model across tofu is constructed in Section 4.2. Finally, in Section 5, the detailed model in the real biological environment corresponding to the second and third scenarios are specified.

2. Acoustic radiation force

The momentum exchange in the scattering process of the incident wave with the particle will cause the ARF acting on the particle [27]. For the theoretical study of the ARF, it can date back to the early work of acoustic radiation pressure and force acting on a spherical particle in an acoustic field in inviscid fluids [28,29]. With the development of ARF calculation theory and acoustic transducers [30–33], it has become a hotspot to employ ARF to selectively manipulate the particle [34]. The basic principle is to create the ARF as the 3D restoring force on the particle in the radiated acoustic field. For the specific target particle, the bubble has large buoyancy in fluid without apparent mass [35]. In order to manipulate the bubble, it is essential to balance the buoyancy of the bubble by the vertical component of the ARF. Meanwhile, the transverse component of the ARF, as a restoring force, traps the bubble [24].

In this paper, we need to achieve the non-contact bubble manipulation across the layered mediums in the real biological environment. According to the origin of ARF, the start point is to analyze the total acoustic field including the scattered and incident acoustic field around the bubble. For the arbitrary incident beam, the decomposition method is often used to compute its scattering with the bubble, which decomposes the incident beam into the elementary waves whose scattering with bubble is known such as the spherical wave in the multipole expansion method (MEM) and plane wave with different propagation direction in the ASM [24,30,36]. And, the equivalence between MEM and ASM in ARF calculation has been demonstrated [37]. Because the plane wave is computed easily and the ASM fits the analysis for the acoustic field radiated by the planar transducer [22], we choose the ASM to calculate the 3D ARF for the required incident beam with bubble in the required environment by our homemade Matlab code [38], which is supplemented with the layered mediums' analysis. The entire ASM-based ARF calculation in this paper aims at trapping a spherical bubble in the unified fluid or real biological layered mediums. The background fluid containing the bubble is assumed as the homogeneous medium when the elementary plane wave in the ASM propagates and the process of ARF calculation is regarded as the steady state in the adiabatic condition, which means that the bubble is a static fluid scatterer.

2.1. ARF on the bubble in unified and undamped fluid

Here, we briefly review the ASM-based ARF formulas on the bubble in a free and ideal fluid space. Following the ASM [30,36], the incident field $p_i(x, y, 0)$ in the source plane ($z = 0$) can be decomposed into a superposition of plane waves with different propagation directions by applying a 2D fast Fourier transform (FFT) from the spatial to the wavenumber domain. It will yield the angular spectrum $S(k_x, k_y)$ distribution in the source plane, which characterizes the amplitudes of every elementary plane wave component. The specific expression is as follows:

$$S\left(k_x, k_y\right) = \int_{-\infty}^{+\infty}\int_{-\infty}^{+\infty} p_i(x, y, 0)e^{-ik_x x - ik_y y}dxdy \tag{1}$$

where, k_x and k_y are the x, y component of each elementary wave vector $\mathbf{k}$ for the source plane field, respectively. When the incident beam in the source plane propagates along the z axis, the angular spectrum $S(k_x, k_y)_{z=0}$ of each elementary plane wave will multiply by the corresponding plane-wave propagation factor $e^{ik_z z}$ in z direction at a z value. Then, we will obtain the $S(k_x, k_y)|_{z=z}$ in any one xy target plane along the z axis. It can be transformed into the 2D pressure distribution in corresponding plane through the inverse fast Fourier transform (IFFT), which is the final result about the incident acoustic field in free space. Thereinto, k_z and k satisfy the relationship $k_z = \sqrt{k^2 - k_x^2 - k_y^2}$. Then, in order to analyze the scattering of spherical bubbles, the spherical coordinate system (r, θ, φ) is selected to expand the incident acoustic field into spherical harmonics combining with the Legendre addition theorem to have a suitable form for scattering solving [30]. The concrete expanding form of incident acoustic field is as follows

$$p_i = \frac{1}{\pi}\sum_{n=0}^{\infty} i^n j_n(kr)\sum_{m=-n}^{n} Y_{nm}(\theta, \varphi) \times \iint_{k_x^2+k_y^2\le k^2} dk_x dk_y S\left(k_x, k_y\right) Y_{nm}^*\left(\theta_k, \varphi_k\right) \tag{2}$$

where $j_n(kr)$ is the spherical Bessel function of the first kind. And the incident angle θ_k and azimuth φ_k of each elementary wave can be calculated by $\cos\theta_k = \sqrt{1 - (k_x^2 + k_y^2)/k^2}$ and $\varphi_k = \arctan(k_y/k_x)$, respectively. Symbol * represents conjugation. Moreover, the expression of the spherical harmonics $Y_{nm}(\theta, \varphi)$ is

$$Y_{nm}(\theta, \varphi) = \sqrt{\frac{(2n+1)}{4\pi}\frac{(n-m)!}{(n+m)!}} P_n^m(\cos\theta)e^{im\varphi} \tag{3}$$

Here, $P_n^m(\cos\theta)$ is the associated Legendre function.

According to the known result of the bubble scattering problem with the plane wave, the corresponding scattering acoustic field also can be obtained and is

$$p_s = \frac{1}{\pi}\sum_{n=0}^{\infty} i^n c_n h_n^{(1)}(kr) \sum_{m=-n}^{n} Y_{nm}(\theta,\varphi) \times \iint_{k_x^2+k_y^2\le k^2} dk_x dk_y S\left(k_x,k_y\right) Y_{nm}^*\left(\theta_k,\varphi_k\right) \tag{4}$$

where $h_n^{(1)}(kr)$ is the spherical Hankel function of the first kind and c_n is scattering coefficient of the bubble with the incident plane wave, which is given as [39]

$$c_n = -\frac{\rho_1 k j_n(k_1 a) j_n'(ka) - k_1 \rho_0 j_n'(k_1 a) j_n(ka)}{\rho_1 k j_n(k_1 a) h_n^{(1)'}(ka) - \rho_0 k_1 j_n'(k_1 a) h_n^{(1)}(ka)} \tag{5}$$

where a is the radius of the target bubble, and k and ρ_0 are the wavenumber and density of the fluid medium around the bubble, respectively. Moreover, k_1 and ρ_1 are wavenumber and density of the air in the bubble, respectively. In the Eqs. (2) and (4), ASM-based beam shape coefficient H_{nm} is introduced. It gives

$$H_{nm} = \iint_{k_x^2+k_y^2\le k^2} dk_x dk_y S\left(k_x,k_y\right) Y_{nm}^*\left(\theta_k,\varphi_k\right) \tag{6}$$

From the Eq. (6), we can find that the H_{nm} can be determined only by the incident beam. Combining with the incident field and scattered field, the total acoustic field $p = p_i + p_s$ can also be obtained.

As described above, when the total acoustic field including the scattered and incident acoustic field around the bubble in the free space is acquired, the ARF exerted on the bubble has been determined. Combining with far-field approximation value of p and the particle vibration velocity $\boldsymbol{v} = \nabla(p/(ikc\rho))$ around the bubble, the final results for the 3D ARF on bubble in the total acoustic field is shown as follows [30]

$$F_x = \frac{1}{8\pi^2\rho c^2 k^2}\,\mathrm{Re} \times \left\{\sum_{n=0}^{\infty}\Psi_n \sum_{m=-n}^{n} A_{nm}\left(H_{nm}H_{n+1,m+1}^* - H_{n,-m}H_{n+1,-m-1}^*\right)\right\} \tag{7}$$

$$F_y = \frac{1}{8\pi^2\rho c^2 k^2}\,\mathrm{Im} \times \left\{\sum_{n=0}^{\infty}\Psi_n \sum_{m=-n}^{n} A_{nm}\left(H_{nm}H_{n+1,m+1}^* + H_{n,-m}H_{n+1,-m-1}^*\right)\right\} \tag{8}$$

$$F_z = -\frac{1}{4\pi^2\rho c^2 k^2}\,\mathrm{Re}\left\{\sum_{n=0}^{\infty}\Psi_n \sum_{m=-n}^{n} B_{nm}H_{nm}H_{n+1,m}^*\right\} \tag{9}$$

where ρ and c are density and velocity of fluid medium around the bubble, respectively. And Ψ_n includes the scatter information between the incident field and the bubble, which is described as

$$\Psi_n = (1+2c_n)(1+2c_{n+1}^*) - 1 \tag{10}$$

Moreover, $A_{nm} = \sqrt{(n+m+1)(n+m+1)/(2n+1)(2n+3)}$ and $B_{nm} = \sqrt{(n+m+1)(n-m+1)/(2n+1)(2n+3)}$.

2.2. ARF on the bubble across the layered mediums

According to the ARF calculation formula in the free space described above, it is essential to obtain the ASM-based beam shape coefficient H_{nm} and scattering coefficient c_n for getting the ARF on the bubble. The H_{nm} can be determined only by the incident beam. When the incident beam propagates through the layered mediums, the acoustic field around the bubble will be altered by transmission, refraction and attenuation [24,25], which will cause the variation of H_{nm}. To be specific, from the calculation Eq. (6) of H_{nm}, it is evident to find that $S(k_x,k_y)$ in the wavenumber domain plane is affected by the transmission and attenuation of the layered mediums and the spherical harmonics $Y_{nm}(\theta_k,\varphi_k)$ is changed by the refraction-caused variation of the incident angle for every elementary plane wave. Here, we will suppose a scenario conforming to our requirement to derive the change of H_{nm} by the layered mediums. Firstly, the pressure distribution of the source plane ($z = 0$) is still supposed to be $p_i(x,y,0)$ and the layered mediums in the fluid will be assumed to be one material layer with the specific loss factor α and thickness d, which has the infinite xy dimension and separates the fluid into upper and lower two layers. Then, the incident beam radiated by the source plane in the upper fluid propagates through the layered mediums along with the z axis and scatters with the bubble behind the material layer.

As the calculation step described in Section 2.1, the incident beam in source plane will be decomposed into superposition of the elementary plane wave and get every corresponding angular spectrum $S(k_x,k_y)$ by the 2D Fourier transform. When the incident beam propagates along z axis and approaches the material layer, $S(k_x,k_y)|_{z=0}$ is multiplied by the corresponding plane-wave propagation factor $e^{ik_z z}$ in z direction at a z value. Then, $S(k_x,k_y)|_{z=z_s}$ outside the upper plane surface of the material layer can be obtained, which is described as $S(k_x,k_y)|_{z=0}e^{ik_z z_s}$. Owing to the transmission at this fluid-material interface, $S'(k_x,k_y)|_{z=z_s}$ inside the upper plane surface of the material layer can be acquired as

$$S'(k_x,k_y)|_{z=z_s} = S(k_x,k_y)|_{z=z_s} \times t_1(\theta_k) \tag{11}$$

Here, $t_1(\theta_k)$ is the pressure transmission coefficient for different incident angle θ_k of every elementary plane wave from fluid to material layer. Meanwhile, the incident angle for every elementary plane wave in the material layer is changed to θ_k', which is given as

$$\theta_k' = \arcsin(\sin(\theta_k)/n_1) \tag{12}$$

This formula is governed by the Snell law [40] and n_1 is the ratio of the velocity for fluid and material layer. Based on these incident angles, the acoustic field inside the material layer continues to propagate in the material layer. Owing to the loss in the material layer, the wave vector $\boldsymbol{k}' = (k_x', k_y', k_z')$ will become $\boldsymbol{k}' + i\boldsymbol{\alpha} = (k_x' + i\alpha_x, k_y' + i\alpha_y, k_z' + i\alpha_z)$ and $S'(k_x,k_y)|_{z=z_s}$ is multiplied by the corresponding plane-wave propagation factor $e^{i(k_z'+i\alpha_z)(z-z_s)}$ in z direction at a z value. However, the xy displacement component of every elementary plane wave will also generate the attenuation when the whole acoustic field propagates along the z axis and can be considered by θ_k' and φ_k relationship with the displacement along z. The concrete angular spectrum of any xy plane in the material layer can be expressed as

$$S'(k_x',k_y')|_{z=z} = S'(k_x,k_y)|_{z=z_s} \times e^{ik_z'(z-z_s)} \times e^{-\alpha_x x_1 - \alpha_y y_1 - \alpha_z z_1} \tag{13}$$

From here, $\alpha_x = \alpha\sin(\theta_k')\cos(\varphi_k)$, $\alpha_y = \alpha\sin(\theta_k')\sin(\varphi_k)$ and $\alpha_z = \alpha\cos(\theta_k')$ are the x, y, z component of α in the material layer for every elementary plane wave. $z_1 = z - z_s$ and x_1 is the propagation distance of every elementary plane wave in x direction, which can be calculated as $x_1 = z_1\tan(\theta_k')\cos(\varphi_k)$. Meanwhile, y_1 is the propagation distance in y direction and is equal to $z_1\tan(\theta_k')\sin(\varphi_k)$. Following this propagation model, the angular spectrum $S'(k_x',k_y')|_{z=z_d}$ inside the lower plane surface of the material layer can be obtained as

$$S'(k_x',k_y')|_{z=z_d} = S'(k_x,k_y)|_{z=z_s} \times e^{ik_z'd} \times e^{-\alpha_x\tan(\theta_k')\cos(\varphi_k)d - \alpha_y\tan(\theta_k')\sin(\varphi_k)d - \alpha_z d} \tag{14}$$

In a similar way, $S''(k_x',k_y')|_{z=z_d}$ outside the lower plane surface of the material layer can be obtained by the pressure transmission coefficient $t_2(\theta_k')$ from material layer to fluid, so

$$S''(k_x',k_y')|_{z=z_d} = S'(k_x',k_y')|_{z=z_d} \times t_2(\theta_k') \tag{15}$$

Upon re-entering the fluid, the incident angle for every elementary plane wave is changed to θ_k and the angular spectrum $S''(k_x,k_y)|_{x=x_0,y=y_0,z=z_0}$ of the target plane center on the bubble (x_0,y_0,z_0) in the lower fluid can be gained as

$$S''(k_x,k_y)|_{x=x_0,y=y_0,z=z_0} = S''(k_x',k_y')|_{z=z_d} \times e^{i(k_x x_0 + k_y y_0 + k_z(z_0 - z_d))} \tag{16}$$

If the lower fluid is added with the specific loss factor α_1, the angular spectrum $S''(k_x, k_y)|_{x=x_0,y=y_0,z=z_0}$ can be modified as

$$S''(k_x, k_y)|_{x=x_0,y=y_0,z=z_0} = S''(k'_x, k'_y)|_{z=z_d} \times e^{i(k_{1x}x_0+k_{1y}y_0+k_{1z}(z_0-z_d))} \times e^{-\alpha_{1x}(z_0-z_d)\tan(\theta_k)\cos(\varphi_k)-\alpha_{1y}(z_0-z_d)\tan(\theta_k)\sin(\varphi_k)} \tag{17}$$

where k_{1x}, k_{1y} and k_{1z} is equal to $k_x + i\alpha_{1x}$, $k_y + i\alpha_{1y}$ and $k_z + i\alpha_{1z}$, respectively. And, $\alpha_{1x} = \alpha_1 \sin(\theta_k)\cos(\varphi_k)$, $\alpha_{1y} = \alpha_1 \sin(\theta_k)\sin(\varphi_k)$ and $\alpha_{1z} = \alpha_1 \cos(\theta_k)$ are the xyz component of α_1 for every elementary plane wave. Finally, based on the angular spectrum in the target plane, we can gain the precise ASM-based beam shape coefficient H_{nm} affected by this layered mediums, which is

$$H_{nm} = \iint_{k_x^2+k_y^2\le k^2} dk_x dk_y S''(k_x, k_y)|_{x=x_0,y=y_0,z=z_0} Y_{nm}^*(\theta_k, \varphi_k) \tag{18}$$

The scattering coefficient c_n for the bubble is calculated by Eq. (5) and this H_{nm} can be directly put into the ARF component calculation Eq. (7), Eqs. (8) and (9). Then, the precise 3D ARF calculation result on the bubble in this scenario can be obtained.

In this section, we derived the Eq. (18) for H_{nm} across the one material layer with the specific loss factor and thickness in fluid. Analogously, if we repeat the step which is to get the angular spectrum and refraction angle of every elementary plane wave across the interface and the reduction for the angular spectrum under the effect of specific loss factor in the material and fluid, H_{nm} across the arbitrary layered mediums with loss factor can also be acquired precisely. Subsequently, combining with the scattering coefficient c_n obtained by the Eq. (5), the final result of ARF on the bubble across corresponding layered mediums can be worked out.

3. Layered mediums with typical biological parameters

3.1. Typical biological parameters and transmission coefficient for layered mediums

The aim of this research is to achieve the bubble selective manipulation across the layered mediums of real biological environment in a theoretical calculation model and study the effect of multiple biological mediums for the trapping ARF on the bubble quantitatively. The calculation method is based on the ASM and in Section 2.2, we obtained the ARF calculation method for one arbitrary air sphere bubble with the arbitrary incident acoustic beam across the one material medium, which can also be extended to the arbitrary layered mediums. In order to match the real biological environment and get the meaningful result for the reference to the biomedicine experiment and application about non-contact bubble manipulation, the layered mediums and fluid in the ARF calculation method need to be specified as the biological tissue materials.

In this paper, we select three scenarios which include the basic biological and experimental environment about non-contact bubble manipulation in vivo and vitro. For the first scenario, the layered mediums are the tofu in the water under 20°C. The incident beam in the source plane propagates from water to tofu and then, comes back to the water. This scenario is a theoretical calculation model supplement for the bubble trapping experiment across the tofu in water [24]. The layered mediums in the second scenario are the fat and muscle which separate the interstitial fluid and water layer. The incident beam propagates from water layer to fat layer, then, from fat layer to muscle layer and finally, to interstitial fluid. It is a real biological environment, which is applied to the pancreas treatment simulation by the high focused ultrasound [26]. In this real scenario, the water is maintained at 20°C, while the biological tissues (the remaining mediums) are at the normal human body temperature of 37°C. Meanwhile, compared with the second scenario, the layered mediums in third scenario are supplemented with the skin layer. The incident beam propagates from the water layer to skin layer and then, like the route in the second scenario. The supplemented skin is also 37°C. According to the paper [26], the third scenario is the most comprehensive biological environment, which can reach any organ like the spleen and duodenum. The concrete and required acoustic properties in three scenarios are listed in Table 1, which is used for ARF calculation acting on the bubble across these specific layered mediums.

Table 1
Acoustic properties of the fluid and layered mediums in three scenarios with density (ρ), longitudinal sound speed (c), and loss factor (α). The incident beam frequency in source plane is f (MHz).

Material	ρ (kg/m^3)	c (m/s)	α (Np/m)
Water [24]	1000	1485	...
Tofu [41]	1010	1507.1	$6.45f^{1.3}$
Skin [26]	1120	1613	$18.08f$
Fat [26]	950	1478	$6.79f^{1.53}$
Muscle [26]	1050	1547	$6.79f^{1.53}$
Interstitial fluid [42]	1020	1520	$3.45f$

Based on the ARF calculation method in Section 2.2, it is essential to calculate the pressure transmission coefficient of every elementary plane wave in the interface of adjacent two material layers along the propagation direction, like $t_1(\theta_k)$ and $t_2(\theta'_k)$. Therefore, in order to achieve the ARF calculation in the established biological and experimental environment, we need to figure out the pressure transmission coefficient under θ_k of every elementary plane wave at the interfaces of three scenarios, according to acoustic properties in Table 1.

For this pressure transmission coefficient calculation, we consider the incident angle between 0° and 90°, which can contain all cases about θ_k of every elementary plane wave in the wavenumber domain plane. Moreover, owing to the acoustic impedance of water and the other mediums in the three scenarios being very close, we can regard these layered mediums and interstitial fluid as the fluid medium [43]. It means that the transverse wave velocity about these mediums does not need to be considered as shown in Table 1. The concrete calculation formula for the fluid-to-fluid pressure transmission coefficient t under θ_k of the element plane wave is as follows [40]

$$t = \frac{p_t}{p_i} = \frac{2m\cos(\theta_k)}{m\cos\theta_k + \sqrt{n^2 - \sin^2\theta_k}} \tag{19}$$

where p_t and p_i are the transmission and incident acoustic pressure of the element plane wave, respectively. And, m is the ratio of the density for adjacent two material layers along the propagation direction of every elementary plane wave, which is described as ρ_2/ρ_1. Meanwhile, n is the ratio of the velocity for adjacent two material layers against the propagation direction and is expressed as c_1/c_2. Based on this formula, using the acoustic properties of tofu and water from Table 1, the plane-wave pressure transmission coefficient for the interface of the first scenario from incident angle $\theta_k = 0°$ to 90° can be obtained. The result is shown in Fig. 1(a). Similarly, the coefficients for the interface of the second and third scenarios from $\theta_k = 0°$ to 90° can also be acquired. The result for the second scenario shown in Fig. 1(b) includes three interfaces' transmission along the propagation direction. Fig. 1(c) is the result for the third scenario with four interfaces' transmission. In Fig. 1, some curves for the plane-wave pressure transmission coefficient are cut off at a certain angle, which means that the elementary plane wave at this incident angle will undergo total internal reflection in the corresponding interface. And then, when the incident angle is larger than this critical angle, the coefficient will become zero.

3.2. The verification for ASM-based ARF calculation method across layered mediums

In Section 3.1, we define the layered mediums and fluids to match the real biological and experimental environment. And, the result for

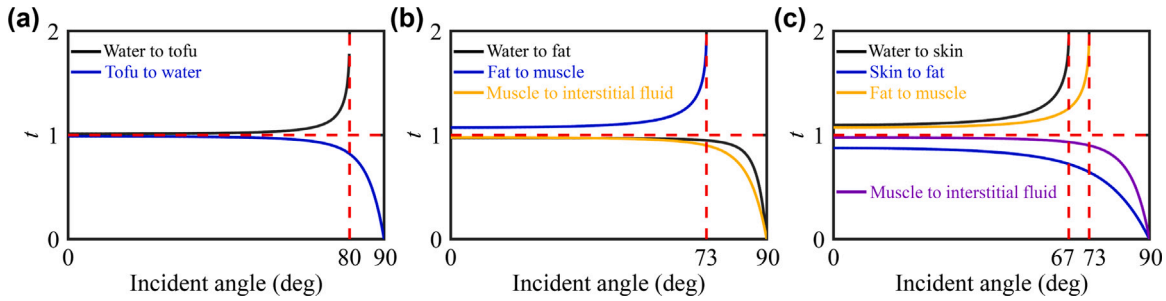

Fig. 1. Plane-wave pressure transmission coefficient t vs. incident angle θ_k from 0° to 90° for three scenarios. The horizontal axis is the incident angle, and the vertical axis is the sound pressure transmission coefficient t. (a) Water and Tofu: Black curve (water to tofu), blue curve (tofu to water). The horizontal red dash line indicates a transmission coefficient of 1; the vertical red dash line marks total reflection at 80°. (b) Water, Fat, Muscle, Interstitial fluid: Black curve (water to fat), blue curve (fat to muscle), yellow curve (muscle to interstitial fluid). The horizontal red dash line indicates a coefficient of 1; the vertical red dash line marks total reflection at 73°. (c) Water, Skin, Fat, Muscle, Interstitial fluid: Black curve (water to skin), blue curve (skin to fat), yellow curve (fat to muscle), purple curve (muscle to interstitial fluid). The horizontal red dash line indicates a coefficient of 1; the vertical red dash lines mark total reflection at 67° and 73°, respectively.

the plane-wave pressure transmission coefficient in three scenarios has been obtained. From the ARF calculation across the layered mediums described in Section 2.2, if we specify the thickness and position of these layered mediums, the size of the bubble and the incident beam in the source plane, the ARF on the bubble across these layered mediums can be worked out. In this way, the theoretical calculation model for ARF across the layered mediums can be established.

Based on the corresponding calculation model, a demonstrating process is conducted to confirm the validity of the ASM-based ARF calculation method across the layered mediums described in Section 2.2. For the first scenario, we suppose that the thickness d_1 of the tofu is 10 mm, which has infinite extent in the xy-plane and separates the water into the upper and lower layer. The source plane ($z = 0$) in the upper water has a 5 mm vertical distance h_1 away from the upper surface of the tofu layer. Moreover, the acoustic source in the source plane is configured to radiate plane waves toward the tofu at incident and azimuth angles of $\theta_k = 45°$ and $\varphi_k = 45°$, with the excitation frequency 2.25 MHz and the original incident pressure 0.02 MPa. In the ASM, the angular spectrum plane still propagates along the z axis and scatters with the bubble in the lower water behind the tofu. The schematic diagram of the model is shown as Fig. 2(a).

In fact, the validity of the ARF calculation method across the layered mediums hinges on the accurate determination of the ASM-based beam shape coefficients, H_{nm}, at the bubble's location. These coefficients are dictated by the incident acoustic field surrounding the bubble. Therefore, the accuracy for the method is verified by comparing the result of the incident acoustic field behind the tofu in the ASM with the result in the numerical simulation. In the ASM, the plane wave field in the source plane at a 45° incident angle is transformed into the angular spectrum and then, the process of the angular spectrum propagating to the plane in the lower water behind the tofu along the z axis is conducted following the procedure described in Section 2.2. The plane-wave pressure transmission coefficient of the specific incident angle, and acoustic properties c and α for tofu and water are obtained from Section 3.1 and Table 1. When obtaining the angular spectrum in any plane behind the tofu, we can calculate the incident acoustic field behind the tofu by the 2D inverse Fourier transform. Meanwhile, in the simulation, we establish the numerical model corresponding to the supposed model and employ the pressure acoustic physics field in the frequency domain to calculate the incident acoustic field behind the tofu in COMSOL Multiphysics 6.1. Finally, the results from both the ASM and the simulation are obtained, as shown in Fig. 2(b). From Fig. 2(b), we can find that the incident acoustic field (the pressure amplitude $|P|$ (Pa) distribution with propagation distance z) behind the tofu in this supposed model is identical in the ASM and simulation, which can demonstrate that the ASM-based ARF calculation method in the first scenario is correct. Similarly, this method can also be confirmed to be correct in the other two scenarios. In conclusion, it is appropriate for this paper to employ this ASM-based ARF calculation method to calculate the selective bubble manipulation across the three kinds of layered mediums in Section 3.1.

4. Bubble manipulation in a unified medium

4.1. Bubble selective manipulation by the focused vortex in the free and undamped water

In Section 3.2, we completed the verification of the ASM-based calculation method for the ARF on the bubble across the layered mediums and can calculate the bubble trapping in the real biological environment. Owing to the distinctive characteristics of the bubble in the fluid, a appropriate acoustic source in the model is significant to create the single-beam 3D selective acoustic tweezers for the bubble 3D selective manipulation. The holographic acoustical tweezer (HAT) in Ref. [36] can produce the 3D radiation selective trap for microparticles and cells in the free and undamped space. However, it is not used to selectively manipulate the bubble, yet. In this paper, we will try this planar and finite aperture transducer more suitable for the ASM to selectively manipulate the bubble.

The HAT shown in Fig. 3(a) is in the source plane ($z = -32$ mm), designed at a frequency $f_0 = 1.2398$ MHz, and the aperture angle and the focus length are 65° and 32 mm, respectively. Based on it, we construct the theoretical calculation model for the trapping of the bubble in the free and undamped fluid space by the ASM-based ARF Eqs. (7), (8) and (9). In this model, the HAT acts as the acoustic source, generating a focused vortex beam at a frequency of 1.2398 MHz with an incident pressure of 7.4 kPa at the source plane. The vortex beam subsequently propagates through 20°C water along the z axis, from the source plane to a downstream plane 64 mm away, where it scatters upon encountering the bubble. The radius of the bubble is 0.1λ and $\lambda = c_w/f_0$ in which c_w is the sound speed of the water as shown in Table 1. The schematic diagram of the model is shown as Fig. 3(a). Under this model, the detailed calculation process is to calculate the z component of the ARF (axial ARF F_z (N)) on the bubble along the z axis in the region of 7.5 mm from the focus point ($z = 0$ mm) firstly, and then, compare the buoyancy of the bubble with the F_z to obtain the axial equilibrium point z_{trap} where the buoyancy equals to the F_z in z axis. Finally, the lateral ARF (F_x (N)) on the bubble is computed at the axial trap equilibrium position z_{trap}, from −3.75 mm to 3.75 mm along the x axis. Owing to rotational symmetry of the incident vortex beam, the F_x can represent all of the lateral ARFs (restoring forces). And we can search the lateral equilibrium point where the $F_x = 0$ in x axis. Generally, there are always two axial equilibrium points in z axis. In the most cases, the axial equilibrium point located at the downstream

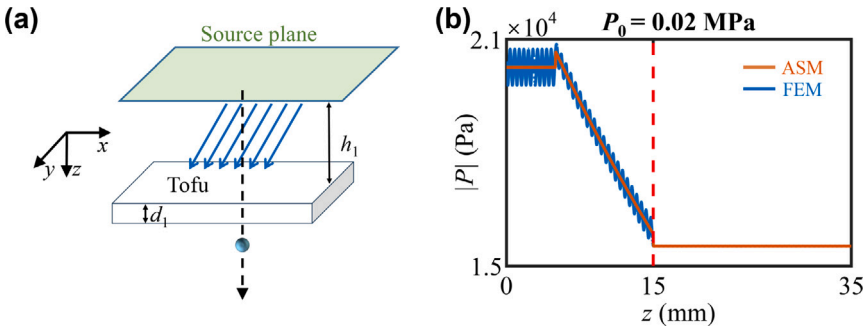

Fig. 2. The across-medium ARF calculation method validation based on the model for an obliquely incident plane wave on Tofu in water. (a) Schematic of the numerical model. A plane wave (blue arrow) is incident at $\theta_k = 45°$, $\varphi_k = 45°$ onto a tofu block submerged in water. The wave propagates through the tofu and scatters with the bubble located in the water below. The sphere represents the bubble, and the white rectangular block is the tofu ($h_1 = 5$ mm, $d_1 = 10$ mm). (b) Comparison of results in the ASM and in the numerical simulation. The incident pressure amplitude $|P|$ (Pa) as a function of propagation distance z (mm) from the source plane is computed using both the ASM and finite element method (FEM), for an incident plane wave with $P_0 = 0.02$ MPa. The field behind the tofu spans from 15 mm to 35 mm, with the red dashed line marking the tofu's lower surface. In the FEM results, multiple scattering at interfaces causes oscillations in the total pressure amplitude before the wave exits the tofu.

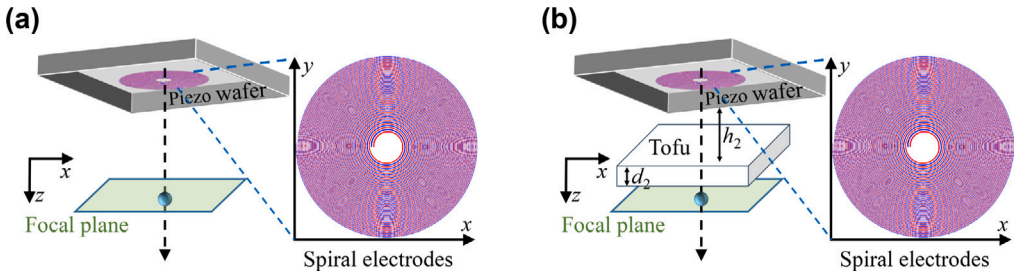

Fig. 3. The schematic diagram of the theoretical calculation model for the trapping of the bubble. (a) The theoretical calculation model for the trapping of the bubble in the free and undamped fluid space is constructed. In the source plane, a one-sided HAT in the piezo wafer radiates the focused acoustic vortex beam along the z axis to scatter with the bubble near the focal plane. It is shown in the red and blue intertwined spiraling electrodes with 35 turns and the details of the HAT, see Ref. [36]. The sphere represents the bubble. (b) The theoretical calculation model for the trapping calculation of the bubble across the tofu layered mediums is established. Compared with (a), the model is inserted by a tofu. For this tofu, the distance away from the source h_2 is 5 mm and the thickness d_2 is 25 mm.

from the focus point ($z > 0$) along the propagation axis is stable. Meanwhile, the steady lateral equilibrium point always occurs near the axial equilibrium point. It should be noted that when employing the ARF formula to compute the theoretical calculation model, the angular spectrum $S(k_x, k_y)$ calculating the H_{nm} in the ARF formula should be in the plane centered at the bubble. The modifying formula is shown as follows

$$S(k_x, k_y)|_{x=x_0, y=y_0, z=z_0} = S(k_x, k_y)|_{z=-32\,\mathrm{mm}} \times e^{i(k_x x_0 + k_y y_0 + k_z(z_0+32\,\mathrm{mm}))} \quad (20)$$

where (x_0, y_0, z_0) is the center position of the bubble. And $k = (k_x, k_y, k_z)$ is the wavenumber in the water, which can be given as $2\pi f_0 / c_w$. When the process is conducted, the result for the axial ARF (F_z (N)) distribution curve and the lateral ARF (F_x (N)) distribution curve is shown in Fig. 4(a). As shown in Fig. 4(a), we can find that the bubble at this size can be trapped by the incident focused vortex beam. And the trapped position is nearly at the axial equilibrium point (z_{trap} = 1.489 mm) in the z axis. Moreover, from the F_x (N) distribution curve in Fig. 4(a), the focused vortex can selectively trap a target bubble, which is the result of the change for sign of F_x (N) around the z_{trap} along x axis. In conclusion, a great single-beam 3D selective acoustic tweezer we need for the bubble in the free water space has been created.

4.2. Bubble selective manipulation verification across tofu based on the model of the unified medium

The performance of the HAT as acoustic source has been proved based on Section 4.1. It can meet our demand to selectively manipulate the bubble in the free and undamped fluid space. To achieve the bubble selective manipulation across the layered mediums of real biological environment, it is natural for us to use the HAT to generate a selective 3D acoustic tweezer across the layered mediums. However, owing to the effect of layered mediums like the muscle, skin and fat, the incident focused vortex will be affected by refraction, transmission and attenuation when across the layered mediums, and can easily become defocused due to distortion, which means that the 3D tweezers created by this acoustic field behind the layered mediums will not be selective anymore [36] and even cannot achieve the 3D trapping under the degenerative axial ARF. Therefore, it is essential to quantitatively study the effect of the layered mediums on the trapping ARF acting on the bubble.

For the better comparison, the first scenario is used for the bubble selective trapping verification across the layered mediums. In this model, a tofu is inserted into the water of 20°C and then, the HAT in the source plane ($z = -32$ mm) radiates the incident focused vortex beam to propagate through the tofu and traps the bubble located on the lower water side. Since the difference between the theoretical calculation model across the medium and in the unified medium is only a piece of the tofu, based on the trapping ARF in the model of the unified medium, the trapping calculation result across the tofu medium can serve as a direct reference to the effect of layer mediums for the trapping ARF on the bubble. Meanwhile, the acoustic properties for the tofu described in Table 1 is similar to the real biological layered mediums, which can mimick the tissue medium in vivo. Thus, the results allow us to deduce the effect of the real biological layered mediums on the trapping ARF.

The specific model for the trapping calculation on the bubble across the tofu layered mediums is shown in Fig. 3(b). Firstly, the same HAT radiates the same focused vortex beam in the same frequency as the

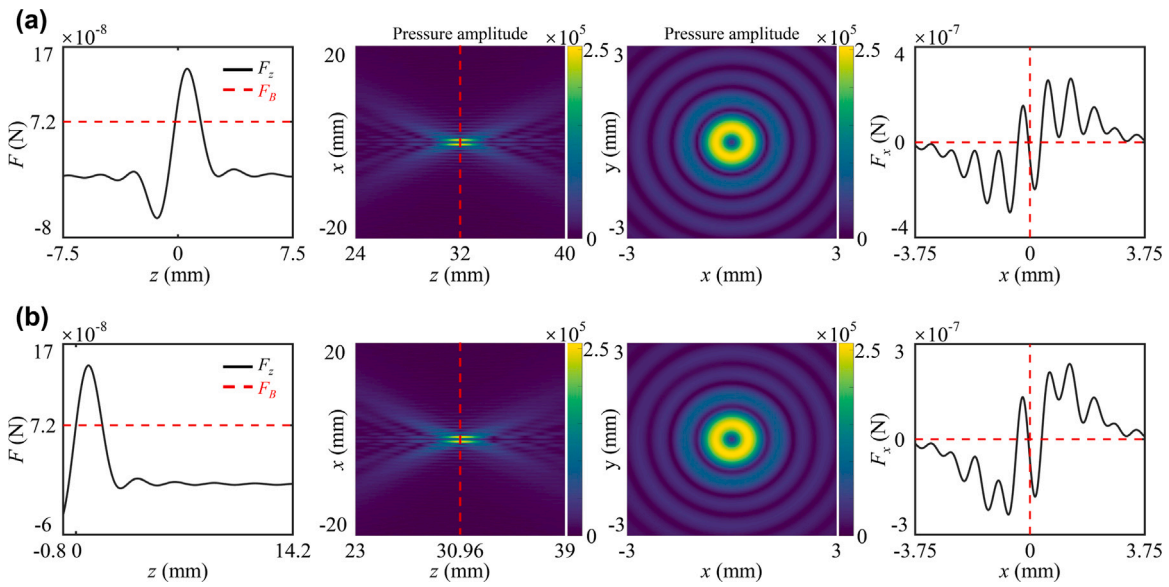

Fig. 4. Bubble trapping analysis in homogeneous and tofu layered media. (a) Homogeneous water medium at 7.4 kPa source incident pressure. Curves in columns 1 and 4 show axial (F_z) and lateral (F_x) radiation forces versus spatial position, respectively. The red dashed line in the axial force profile indicates the bubble buoyancy $F_B = \frac{4}{3}\pi a^3 \rho_w g$, where a is the bubble radius, ρ is the water density, and $g = 10\,(\mathrm{N/kg})$ is the gravitational acceleration. In the lateral force profile, vertical and horizontal dashed lines mark the axial equilibrium position ($x = 0$) and zero force level ($F_x = 0$). Columns 2 and 3 display the pressure amplitude distribution in the propagation plane (left, red line marks focal length) and focal plane (right). (b) Layered tofu mediums at 11.005 kPa source incident pressure. Axial and lateral radiation forces are shown similarly to (a), with adjusted spatial ranges. Pressure field distributions follow the same arrangement as (a), with modified propagation plane coordinates.

model of the unified medium and the focused vortex beam propagates in the water medium before the tofu. Then, the incident focused vortex propagates through the tofu located in the distance of $h_2 = 5$ mm away from the source plane and the thickness is $d_2 = 25$ mm along z axis. Finally, the acoustic field scatters with the same bubble described by the unified medium model in the lower water side. The total propagation distance is 64 mm and direction is along z axis. We employ the ASM-based ARF calculation method across the layered mediums described in Section 2.2 to calculate the bubble trapping ARF in this model. The F_z (N) and F_x (N) computation process for demonstrating bubble whether to be trapped is similar to the trapping calculation in the model of the unified medium. However, owing to the unknown for the trapping result across the tofu, we do not specify the incident acoustic pressure in the source plane of this model. We determined the incident pressure by comparing the maximum amplitude of pressure in the propagation plane (xz plane from $z = -32$ mm to $z = 32$ mm). This approach ensured successful bubble trapping behind the tofu. The pressure amplitude distribution in the propagation plane for the trapping model of the unified medium is shown in the second figure of Fig. 4(a). When the incident pressure in the source plane is 11.005 kPa, we can get the nearly same maximum amplitude of pressure in the propagation plane of the acoustic field for the model across the tofu. The result is shown in the second figure of Fig. 4(b). From this figure, we find that the focus distance is changed to be 30.96 mm by the tofu layered mediums, which means that the focal plane is still behind the tofu and we established a correct model. Therefore, the coordinate for the source plane ($z = -30.96$ mm) is updated. Then, under the incident acoustic pressure for the HAT in this calculation model across the tofu, we can calculate the F_z (N) on the bubble along the z axis in the region of -0.8 mm to 14.2 mm from the focus point ($z = 0$ mm) and the F_x (N) on the bubble at the axial trap equilibrium position z_{trap}, from -3.75 mm to 3.75 mm along the x axis. The result for the F_z (N) and F_x (N) distribution curve is shown in Fig. 4(b), leading to the conclusion that the bubble at the same size behind the tofu can be 3D trapped nearly at the axial equilibrium point ($z_{trap} = 1.724$ mm) in the z axis by the focused vortex across the tofu and the trapping is also selective. A similarly 3D selective acoustic tweezer across the tofu layer mediums like the trapping model of the unified medium has been created under the incident pressure 11.005 kPa for the HAT.

In summary, we can find that when the tofu with the thickness 25 mm is inserted into the water unified medium, for the trapping bubble calculation, the pressure amplitude for the incident focused vortex acoustic field around the target bubble can be attenuated greatly (from 11.005 kPa to 7.4 kPa), which can cause the trapping ARF F_z (N) and F_x (N) to decrease by two to three times. This loss is from the transmission in the interface and the attenuation in the tofu medium. Meanwhile, owing to the refraction in the interface, the focus distance for the focused vortex acoustic field is changed from 32 mm to 30.96 mm. With the focal point getting closer to the source plane, the trapping point z_{trap} will be offset along the z axis. However, the effect of the tofu layered mediums on the vortex focusing is slight. This indicates that the selective manipulation capability is retained when the incident focused vortex acoustic field across the tofu layer mediums.

5. Bubble manipulation in multilayer mediums

In the previous section, we demonstrated that the focused acoustic vortex generated by the HAT can achieve selective bubble trapping in water and through a tofu medium. Since tofu acoustically resembles real tissue, this method is potentially applicable to biomedical applications, though performance depends critically on matching the incident pressure to the medium. Successful trapping through tofu confirms that, with proper acoustic field design tailored to the layered mediums, the HAT may function as an effective 3D acoustic tweezer for bubbles even behind biological barriers.

Generally, the real biological environment includes the multiple biological mediums. We implemented the second and third scenarios to model these complex biological environments according to the Ref. [26]. Following the approach established for the tofu medium, we developed a bubble trapping calculation model for multilayered biological systems, including the fat-muscle structure in Scenario 2. In this model, the incident focused vortex beam radiated by the same HAT of the source plane ($z = -32$ mm) in the same frequency propagates in the 20°C water medium before the fat along the z axis, firstly,

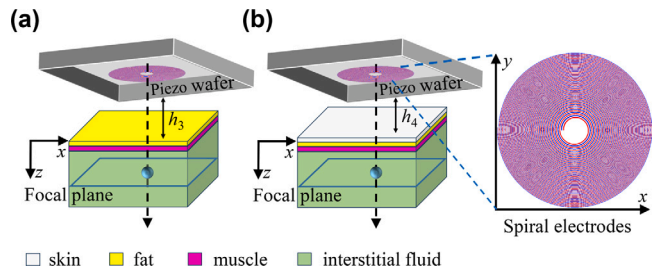

Fig. 5. The schematic diagram of the theoretical calculation model for the bubble trapping in the real biological environment. (a) The theoretical calculation model for the trapping of the bubble across the real biological multilayered mediums such as fat and muscle in the second scenario is constructed. The same HAT in the piezo wafer radiates the focused vortex beam to scatter with the bubble in the green interstitial fluid. And the yellow fat layer with the thickness 20.17 mm is $h_3 = 2.12$ mm away from the source plane in the z direction. Moreover, the adjacent pink muscle layer with thickness 6.58 mm is located above the bubble shown as the blue–green solid particle. (b) The theoretical calculation model for the trapping of the bubble across the real biological multilayered mediums such as skin, fat and muscle in the third scenario is established. Compared with the (a), it adds a white skin layer with the thickness 1.49 mm into the position between the water layer and yellow fat layer. And the h_4 is still 2.12 mm.

and then, propagates through the fat with the thickness 20.17 mm, which is located at the distance 2.12 mm away from the source plane in the z direction. After passing through the fat layer, the focused beam propagates through a 6.58 mm thick muscle layer and reaches the interstitial fluid, where it will scatter with a bubble of radius $a = 0.1c_{inter}/f_0$. Here, c_{inter} is the sound velocity of the interstitial fluid described in Table 1. The total propagation distance is also 64 mm and direction is along z axis. In this way, the schematic diagram of the model can be constructed in Fig. 5(a). And the calculation process for the trapping ARF on the bubble in this model can be based on the similar process in the trapping calculation model across the tofu. We can also decide the incident pressure in the source plane by the way in which the maximum amplitude of pressure in the xz propagation plane (from $z = -32$ mm to $z = 32$ mm) of this model is analogized from the model in the unified water above in the same manner and the value is 11.794 kPa. Then, under this incident pressure for the HAT, the nearly same maximum amplitude of pressure in the propagation plane in this model can be obtained in Fig. 6(a). The focal distance shifts from 32 mm to 31.28 mm, located beyond the muscle layer. Therefore, the position of the source plane is reset to $z = -31.28$ mm, and under this incident pressure, we employ the extended ASM-based ARF calculation method across the layered mediums described in Section 2.2 to calculate the trapping ARF on the bubble in the interstitial fluid. According to the trapping ARF computation step in the calculation model across the tofu, we can acquire the calculation result for the trapping ARF F_z (N) and F_x (N) on the bubble. It includes the F_z (N) on the bubble scattering with the incident focused vortex beam along the z axis in the region of −2.3 mm to 12.7 mm from the focus point ($z = 0$ mm) and the F_x (N) on the bubble at the axial trap equilibrium position z_{trap}, from −3.75 mm to 3.75 mm along the x axis. The distribution curves are shown in Fig. 6(a). Obviously, the bubble at this size in the interstitial fluid has been trapped nearly at the axial trap equilibrium position $z_{trap} = 1.58$ mm in the z axis while retaining selective trapping characteristics. Combining with the similar trapping ARF, it demonstrates that the similarly 3D selective acoustic tweezers across the real biological multilayered mediums in the second scenario can be created under the incident focused vortex radiated by this HAT in an analogical incident pressure. Meanwhile, owing to the transmission of the interface and attenuation in this real biological multilayer mediums, it also results in a significant attenuation of the pressure amplitude for the incident focused vortex acoustic field around the target bubble. Compared with the model in unified medium above, the concrete value is from 11.794 kPa to 7.4 kPa, which means the trapping ARF on the bubble will decrease by two or three times in this real biological multilayer mediums.

For the third scenario, the real multiple biological mediums are inserted with a skin layer based on the second scenario. Thus, the theoretical calculation model for bubble trapping across the multilayered mediums corresponding to this scenario can be established by adding a skin layer with thickness 1.49 mm into the calculation model of the second scenario. The exact position of the skin layer is between 20°C water and fat layer, and 2.12 mm away from the source plane. The schematic diagram of the model is shown in Fig. 5(b). Then, we can calculate this model, according to the trapping calculation process on the bubble for the calculation model belonging to the second scenario. The incident pressure for the same HAT in the source plane is set to be 13.343 kPa and the focal distance is changed from 32 mm to 30.96 mm. When the position of the source plane is reset as $z = -30.96$ mm, we can calculate the trapping ARF of the same bubble in the interstitial fluid under the incident focused vortex beam. The result is the F_z (N) on the bubble along the z axis in the region of −0.5 mm to 14.5 mm from the focus point ($z = 0$ mm) and the F_x (N) on the bubble at the axial trap equilibrium position z_{trap}, from −3.75 mm to 3.75 mm along the x axis, which is shown in Fig. 6(b). Based on the analysis of the F_z (N) and F_x (N) distribution curve in Fig. 6(b), we can find that the bubble at the same size as the second scenario can be trapped nearly at the axial trap equilibrium position $z_{trap} = 1.67$ mm in the z axis and a similarly 3D selective tweezer across the real biological multilayer mediums of the third scenario can be also created by this HAT in an analogical incident pressure. Moreover, in this real biological environment, compared with the unified model above, the pressure amplitude of the incident focused vortex acoustic field around the target bubble will decrease from 13.343 kPa to 7.4 kPa. It also means that in this real biological multilayer mediums, the trapping ARF on the bubble will be further reduced by three or four times, when the skin layer is introduced.

In this section, the non-contact bubble selective manipulation in the real biological environment corresponding to second and third scenarios has been verified and the effect for the trapping ARF has also been analyzed. The attenuation of the pressure amplitude in a focused vortex acoustic field occurs both within the layer mediums and at their interfaces, as demonstrated by the tofu model. This attenuation is further exacerbated in the real biological environment. To ensure comparability, the incident pressure for the same HAT is maintained at a fixed value in all four models. The trapping ARF acting on a bubble in water or interstitial fluid is subsequently calculated by the corresponding method and process. When getting the result for the trapping ARF and the pressure amplitude distribution in the focal plane ($z = 0$), the respective maximum of the axial F_z (N) ARF and the pressure amplitude of the focal plane in these four models will be worked out for comparing. For the intuition, these comparing results are normalized by the maximum in four. Finally, they are directly presented by Fig. 7(a) and (b). From the two figures, we can obviously find that the axial F_z (N) ARF and pressure amplitude of the focal plane will decrease with increasing of layer number for the layered mediums. Compared with the zero layer number in the unified model, the one layer number for the tofu layered mediums will generate the attenuation for the pressure amplitude of the incident focused vortex acoustic field around the target bubble by 1.47 times and the axial F_z (N) ARF on the bubble by 2.14 times. For the two layer number corresponding to the real biological multilayer mediums like the fat and muscle in the second scenario, the attenuation for the pressure amplitude and the axial F_z (N) ARF will increase by 1.52 and 2.25 times, respectively. Moreover, owing to the addition of the skin layer for the real biological multilayer mediums in the third scenario, the attenuation further increases, with the pressure amplitude and ARF reduced by 1.71 and 2.88 times. In conclusion, owing to the consideration of the complicated multilayered mediums in the real biological environment, the attenuation for the

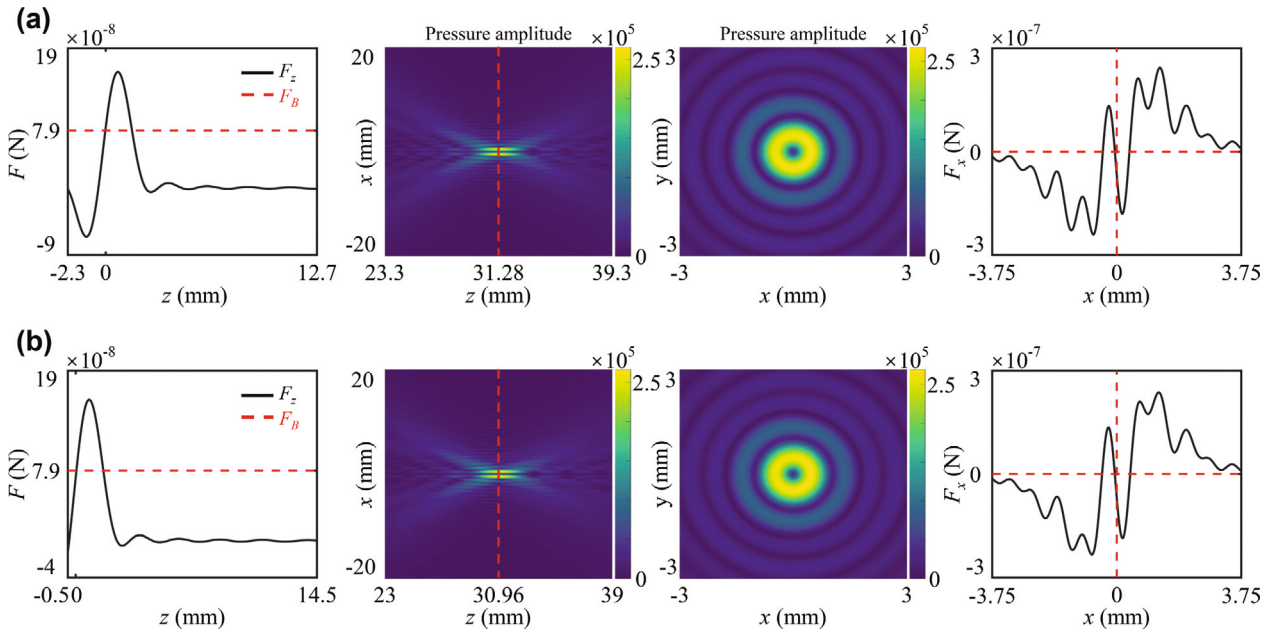

Fig. 6. Bubble trapping analysis in real biological environment of second and third scenarios. (a) Second scenario:Real multilayer tissue mediums including fat and muscle at 11.794 kPa source incident pressure. Curves in columns 1 and 4 show axial (F_z) and lateral (F_x) radiation forces versus spatial position, respectively. The red dashed line in the axial force profile indicates the bubble buoyancy $F_B = \frac{4}{3}\pi a^3 \rho_{inter} g$, where a is the bubble radius, ρ_{inter} is the interstitial fluid density, and $g = 10\,(\mathrm{N/kg})$ is the gravitational acceleration. In the lateral force profile, vertical and horizontal dashed lines mark the axial equilibrium position ($x = 0$) and zero force level ($F_x = 0$). Columns 2 and 3 display the pressure amplitude distribution in the propagation plane (left, red line marks focal length) and focal plane (right). (b) Third scenario:Real skin, fat and muscle tissue layered mediums at 13.343 kPa source incident pressure. Axial and lateral radiation forces are shown similarly to (a), with adjusted spatial ranges. Pressure field distributions follow the same arrangement as (a), with modified propagation plane coordinates.

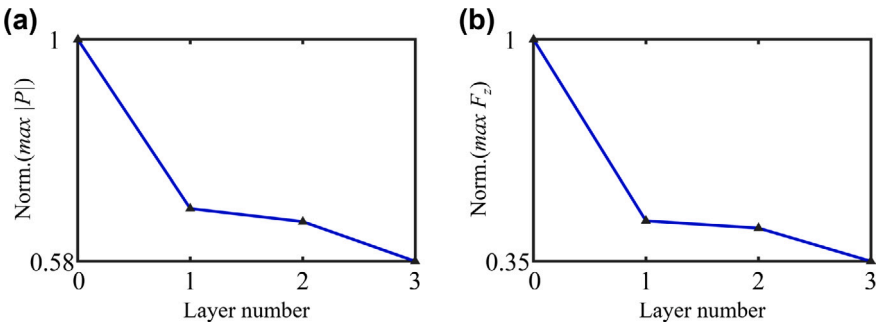

Fig. 7. Normalized maximum values of (a) the focal plane pressure amplitude (Norm.($max\,|P|$) vs. layer number) and (b) the axial (Norm.($max\,F_z$) vs. layer number) ARF on the bubble, as functions of the number of layers in the four calculation models. The incident pressure is kept constant for comparison. Layer numbers 0 and 1 correspond to the uniform and single-layer (tofu) models, respectively, while layers 2 and 3 represent models of the real biological environment. All values are normalized by their corresponding maximum in the four models. Data points (connected by blue lines to show the trend) demonstrate a decrease with increasing layer number.

pressure amplitude of the across-medium 3D selective tweezers acting on the bubble will decrease greatly, which will cause the axial trapping ARF on the bubble to decrease by two to three times. It means that the real biological multilayer mediums will generate great impact on the non-contact bubble manipulation.

6. Summary

In order to supplement the numerical modeling of the ARF on a bubble in the real biological environment, this paper proposes the method for calculating the ARF across the one material medium, which can be extended to any layered mediums. The research focuses on two biologically relevant scenarios for ultrasonic therapy [26], constructing corresponding trapping models based on an extended "across-tofu" framework. Based on the analogy approach mentioned in Section 4.2, we determined suitable incident pressure for the HAT and computed trapping forces by integrating an ASM-based ARF calculation method for layered mediums, similar to trapping calculation model across the tofu. The results demonstrate that a comparable 3D selective trapping effect to that of the unified model can be achieved, albeit with significant attenuation of the incident focused vortex beam. Notably, a stable trapping ARF on the bubble was confirmed in the chosen real biological environment. Moreover, for the four models above, with the same incident pressure, the direct and precise comparison for the effect of the layered mediums was conducted. The similar conclusion and concrete values were obtained, which means that the multilayered mediums definitely generated a great attenuation on the ARF, especially the axial ARF (F_z (N)). In conclusion, this research provides the effect of multiple biological mediums for the trapping ARF on bubbles and the effective model for creating similarly 3D selective tweezer in the real biological environment like the unified model. These outcomes offer a reference for designing acoustic fields, such as determining the incident pressure for transducers like the HAT, in non-contact bubble

manipulation applications. Furthermore, it offers insights for mitigating the influence of real multilayered media on the trapping efficacy.

Nevertheless, it is known that real biological multilayered mediums, such as fat, muscle, and skin, are viscoelastic, which means that in order to better reflect reality, we should consider the propagation and refraction of the transverse and longitudinal plane waves [44] when the incident focused vortex beam across these layered mediums in the ASM. But in this work, all the layered mediums are treated as the fluid medium. Although this is a reasonable simplification according to the Ref. [43], it still introduces errors in the calculated trapping ARF on the bubble across the above layered mediums. Meanwhile, the steady state assumption for the ARF calculation process on the bubble neglects the damping effect of the bubble oscillation. In fact, the pulsating bubble in the viscous medium like the interstitial fluid will be subjected to viscous damping [45] which can reduce the scattering cross-section of the bubble under the elementary plane wave [46] in the ASM and decrease the magnitude of the ARF on the bubble. Moreover, when the elementary plane wave in the ASM reaching the bubble in the water or interstitial fluid, the corresponding plane-wave propagation factor and loss factor should be corrected to the gas's in the bubble and consider the refraction in the bubble surface. In fact, the bubble can change the propagation characteristic of the elementary plane wave, but owing to the limited impact of the one small bubble, the homogeneous background fluid assumption in the propagation will only cause tiny errors to the ARF calculation. In the future, we will revisit the essential properties of the listed biological multilayered mediums and consider their viscoelasticity, combining with the bubble dynamics in the viscous medium and the bubble-caused non-homogeneity of the medium, to comprehensively calculate the across-medium effect for the ARF on the bubble. These more precise results will provide better guidance for the non-contact bubble manipulation in the real biological environment.

CRediT authorship contribution statement

Xuan Cheng: Writing – original draft, Visualization, Validation, Methodology, Investigation, Formal analysis, Data curation, Conceptualization. **Yuehaiqin Wang:** Writing – original draft, Validation, Methodology, Investigation, Formal analysis, Data curation. **Shiyu Li:** Writing – original draft, Data curation. **Zhixiong Gong:** Writing – review & editing, Validation, Supervision, Resources, Project administration, Funding acquisition, Conceptualization.

Declaration of competing interest

The authors declare the following financial interests/personal relationships which may be considered as potential competing interests: Zhixiong GONG reports financial support was provided by The National Natural Science Foundation of China. If there are other authors, they declare that they have no known competing financial interests or personal relationships that could have appeared to influence the work reported in this paper.

Acknowledgments

Z. Gong thanks for the support from the National Natural Science Foundation of China (No. 24Z990200542 and No. 12504522), the Shanghai Jiao Tong University 2030 Initiative, China, the Shanghai Jiao Tong University AI for Engineering Initiative, China, Shanghai Jiao Tong University, China for the startup funding (Nos. WH220401017 and WH22040121), and the XIAOMI Foundation.

Data availability

Data will be made available on request.

References

[1] L. Meng, X. Cui, C. Dong, X. Liu, W. Zhou, W. Zhang, X. Wang, L. Niu, F. Li, F. Cai, et al., Microbubble enhanced acoustic tweezers for size-independent cell sorting, Appl. Phys. Lett. 116 (7) (2020).
[2] J.L. Bull, The application of microbubbles for targeted drug delivery, Expert Opin. Drug Deliv. 4 (5) (2007) 475–493.
[3] J.J. Choi, K. Selert, F. Vlachos, A. Wong, E.E. Konofagou, Noninvasive and localized neuronal delivery using short ultrasonic pulses and microbubbles, Proc. Natl. Acad. Sci. 108 (40) (2011) 16539–16544.
[4] W.-C. Lo, C.-H. Fan, Y.-J. Ho, C.-W. Lin, C.-K. Yeh, Tornado-inspired acoustic vortex tweezer for trapping and manipulating microbubbles, Proc. Natl. Acad. Sci. 118 (4) (2021) e2023188118.
[5] L. Guerassimoff, S.C. De Smedt, F. Sauvage, M. Baudoin, Acoustic tweezers for targeted drug delivery, Adv. Drug Deliv. Rev. (2025) 115551.
[6] C. Errico, J. Pierre, S. Pezet, Y. Desailly, Z. Lenkei, O. Couture, M. Tanter, Ultrafast ultrasound localization microscopy for deep super-resolution vascular imaging, Nature 527 (7579) (2015) 499–502.
[7] G. Zhang, X. Hu, X. Ren, B. Zhou, B. Li, Y. Li, J. Luo, X. Liu, D. Ta, In vivo ultrasound localization microscopy for high-density microbubbles, Ultrasonics 143 (2024) 107410.
[8] D. Bouchet, O. Stephan, B. Dollet, P. Marmottant, E. Bossy, Near-field acoustic imaging with a caged bubble, Nat. Commun. 15 (1) (2024) 10275.
[9] B. Dollet, P. Marmottant, V. Garbin, Bubble dynamics in soft and biological matter, Annu. Rev. Fluid Mech. 51 (1) (2019) 331–355.
[10] D. Denkova, M. Ploschner, M. Das, L.M. Parker, X. Zheng, Y. Lu, A. Orth, N.H. Packer, J.A. Piper, 3D sub-diffraction imaging in a conventional confocal configuration by exploiting super-linear emitters, Nat. Commun. 10 (1) (2019) 3695.
[11] L. Littner, I. Solodov, M. Kreutzbruck, Local defect resonance and nonlinearity of porosity air bubbles in solids, Ultrasonics 142 (2024) 107373.
[12] A. Penneron, T. Brunet, D. Baresch, Active rheology of soft solids performed with acoustical tweezers, Appl. Phys. Lett. 126 (8) (2025).
[13] A. Rezaei, D.F. Rivas, G. Lajoinie, M. Versluis, Modeling nonlinear scattering of phospholipid-coated microbubbles in elastic media, Ultrasonics (2026) 107964.
[14] M.A. Herrada, J.G. Eggers, Path instability of an air bubble rising in water, Proc. Natl. Acad. Sci. 120 (4) (2023) e2216830120.
[15] A. Ashkin, J.M. Dziedzic, J.E. Bjorkholm, S. Chu, Observation of a single-beam gradient force optical trap for dielectric particles, Opt. Lett. 11 (5) (1986) 288–290.
[16] A. Ashkin, Acceleration and trapping of particles by radiation pressure, Phys. Rev. Lett. 24 (4) (1970) 156.
[17] D. Ahmed, C. Dillinger, A. Hong, B.J. Nelson, Artificial acousto-magnetic soft microswimmers, Adv. Mater. Technol. 2 (7) (2017) 1700050.
[18] D. Wu, D. Baresch, C. Cook, Z. Ma, M. Duan, D. Malounda, D. Maresca, M.P. Abundo, J. Lee, S. Shivaei, et al., Biomolecular actuators for genetically selective acoustic manipulation of cells, Sci. Adv. 9 (8) (2023) eadd9186.
[19] G.T. Silva, A.L. Baggio, Designing single-beam multitrapping acoustical tweezers, Ultrasonics 56 (2015) 449–455.
[20] Y. Liu, D. Cheng, G. Sonek, M. Berns, C. Chapman, B. Tromberg, Evidence for localized cell heating induced by infrared optical tweezers, Biophys. J. 68 (5) (1995) 2137–2144.
[21] A. Blázquez-Castro, Optical tweezers: Phototoxicity and thermal stress in cells and biomolecules, Micromachines 10 (8) (2019) 507.
[22] S. Li, Z. Gong, Reversing the acoustic contrast factor by tuning the medium can make focused beams trap cells in three dimensions, Phys. Fluids 37 (1) (2025).
[23] Q. Liu, Q. Tang, J. Hu, A new strategy to capture single biological micro particles at the interface between a water film and substrate by ultrasonic tweezers, Ultrasonics 103 (2020) 106067.
[24] D. Baresch, V. Garbin, Acoustic trapping of microbubbles in complex environments and controlled payload release, Proc. Natl. Acad. Sci. 117 (27) (2020) 15490–15496.
[25] M.A. Ghanem, A.D. Maxwell, Y.-N. Wang, B.W. Cunitz, V.A. Khokhlova, O.A. Sapozhnikov, M.R. Bailey, Noninvasive acoustic manipulation of objects in a living body, Proc. Natl. Acad. Sci. 117 (29) (2020) 16848–16855.
[26] M. Gray, L. Spiers, C. Coussios, Effects of human tissue acoustic properties, abdominal wall shape, and respiratory motion on ultrasound-mediated hyperthermia for targeted drug delivery to pancreatic tumors, Int. J. Hyperth. 39 (1) (2022) 918–934.
[27] M. Settnes, H. Bruus, Forces acting on a small particle in an acoustical field in a viscous fluid, Phys. Rev. E 85 (1) (2012) 016327.
[28] L.V. King, On the acoustic radiation pressure on spheres, Proc. R. Soc. Lond. Ser. A-Math. Phys. Sci. 147 (861) (1934) 212–240.
[29] L.P. Gor'kov, On the forces acting on a small particle in an acoustical field in an ideal fluid, Sov. Phys. Dokl. 6 (1962) 773.
[30] O.A. Sapozhnikov, M.R. Bailey, Radiation force of an arbitrary acoustic beam on an elastic sphere in a fluid, J. Acoust. Soc. Am. 133 (2) (2013) 661–676.
[31] N. Jiménez, V. Romero-García, L.M. García-Raffi, F. Camarena, K. Staliunas, Sharp acoustic vortex focusing by Fresnel-spiral zone plates, Appl. Phys. Lett. 112 (20) (2018).

[32] M. Baudoin, J.-C. Gerbedoen, A. Riaud, O.B. Matar, N. Smagin, J.-L. Thomas, Folding a focalized acoustical vortex on a flat holographic transducer: Miniaturized selective acoustical tweezers, Sci. Adv. 5 (4) (2019) eaav1967.
[33] M. Baudoin, J.-L. Thomas, R.A. Sahely, J.-C. Gerbedoen, Z. Gong, A. Sivery, O.B. Matar, N. Smagin, P. Favreau, A. Vlandas, Spatially selective manipulation of cells with single-beam acoustical tweezers, Nat. Commun. 11 (1) (2020) 4244.
[34] M. Baudoin, J.-L. Thomas, Acoustic tweezers for particle and fluid micromanipulation, Annu. Rev. Fluid Mech. 52 (1) (2020) 205–234.
[35] S.S. Rao, D.S. García, R.R. Figueroa, G.d.V.D. Muñoz, Vibraciones Mecánicas, vol. 776, Pearson educación, 2012.
[36] Z. Gong, M. Baudoin, Three-dimensional trapping and dynamic axial manipulation with frequency-tuned spiraling acoustical tweezers: A theoretical study, Phys. Rev. Appl. 16 (2) (2021) 024034.
[37] Z. Gong, M. Baudoin, Equivalence between angular spectrum-based and multipole expansion-based formulas of the acoustic radiation force and torque, J. Acoust. Soc. Am. 149 (5) (2021) 3469–3482.
[38] Z. Gong, M. Baudoin, Single beam acoustical tweezers based on focused beams: A numerical analysis of two-dimensional and three-dimensional trapping capabilities, Phys. Rev. Appl. 18 (4) (2022) 044033.
[39] P. Martin, Acoustic scattering by one bubble before 1950: Spitzer, Willis, and Division 6, J. Acoust. Soc. Am. 146 (2) (2019) 920–926.
[40] L.E. Kinsler, A.R. Frey, A.B. Coppens, J.V. Sanders, Fundamentals of Acoustics, John wiley & sons, 2000.
[41] Y.T. Kim, H.C. Kim, M. Inada-Kim, S.S. Jung, Y.H. Yun, M.J. Jho, K. Sandstrom, Evaluation of tissue mimicking quality of tofu for biomedical ultrasound, Ultrasound Med. Biol. 35 (3) (2009) 472–481.
[42] R.S. Cobbold, Foundations of Biomedical Ultrasound, Oxford University Press, 2006.
[43] H. Azhari, Basics of Biomedical Ultrasound for Engineers, John Wiley & Sons, 2010.
[44] L.M. Brekhovskikh, O.A. Godin, Acoustics of Layered Media I: Plane and Quasi-Plane Waves, vol. 5, Springer Science & Business Media, 2012.
[45] C. Devin Jr., Survey of thermal, radiation, and viscous damping of pulsating air bubbles in water, J. Acoust. Soc. Am. 31 (12) (1959) 1654–1667.
[46] M.A. Ainslie, T.G. Leighton, Review of scattering and extinction cross-sections, damping factors, and resonance frequencies of a spherical gas bubble, J. Acoust. Soc. Am. 130 (5) (2011) 3184–3208.